Research Article

Weisen Chen, Hai Fang*, Lu Zhu, Xinchen Zhang, and Junyu Zhu

Bending energy absorption performance of composite fender piles with different winding angles

https://doi.org/10.1515/rams-2024-0004 received December 10, 2023; accepted March 01, 2024

Abstract: In recent years, there has been an increase in accidents involving vessels colliding with bridge piers. These ship-bridge collisions can result in tragic loss of life and severe damage to the bridge structure. To address this issue, a type of fender pile made of winding-formed glass fiber-reinforced polymer (GFRP) was proposed as a solution. In this article, three- and four-point bending tests were performed to compare and analyze the damage modes and load-carrying capacity of the fender piles at two different winding angles, namely 45° and 75°. Vertical impact test was simulated using ANSYS/LS-DYNA to verify finite element models. The results revealed variations in damage patterns and bending performance of GFRP piles under the two fiber winding angles. The simulation results suggest that GFRP fender piles can effectively increase the impact time of shipbridge collisions and reduce the collision forces, thereby significantly improving the protection of bridge piers.

Keywords: GFRP, winding angles, fender piles, failure modes, finite element simulation

1 Introduction

Ship—bridge collision accidents have become a significant concern in the field of transportation, with a higher occurrence rate compared to other disasters like earthquakes and typhoons [1,2]. These accidents often lead to catastrophic consequences such as damage to bridge structures, ship sinkings, and casualties [3–5]. Steel fenders

are often used in bridge protections to absorb impact energy associated with a vessel collision [6,7]. However, disadvantages such as susceptibility to corrosion have been evidenced in existing fenders. As a result, bridge—ship collision facilities have garnered significant attention and research in recent years.

Fiber-reinforced polymers (FRP) have gained significant popularity in infrastructure applications due to their advantageous properties, such as design flexibility, lightweight nature, and high strength [8-10]. Fiber winding technology can be used to produce composite pipes with good flexural properties based on different angles and number of layups [11,12]. Cai et al. [13] investigated the effect of different layup angles on the bending performance of composite pipes and found that increasing the winding angle can slow down the failure caused by compression buckling. Vincent and Ozbakkaloglu [14] conducted a force performance study on concrete specimens restrained by FRP pipes with different fiber angles, demonstrating that an increased fiber ring arrangement effectively improved the restraining efficiency of FRP pipes on concrete. However, the confinement method did not notably influence the axial stress-strain behavior of FRPconfined concrete. Zhang et al. [15] conducted axial compression tests on fiber-reinforced concrete-steel composite double-walled pipe columns with different winding angles, indicating a strong bond between the fibers and the pile, and enhanced confinement effects with greater absolute values of the fiber angle. Jin's research indicated that lattice frame reinforcement in syntactic foam-filled glass fiberreinforced polymer (GFRP) tubes contributed to increased compressive strength and energy absorption [16]. Gemi et al. [17–24] studied compressive behavior and failure analysis of reinforced concrete-filled pultruded GFRP composite hybrid beams and glass fiber-reinforced filament wound pipes and investigated the effect of diameter upon low-velocity impact response. The results of the study show that the composite pipe pile has better absorption performance at low-velocity impact. The basic mechanical aspects of compression and bending in FRP pipes have been preliminarily studied, and

Weisen Chen, Lu Zhu, Xinchen Zhang, Junyu Zhu: College of Civil Engineering, Nanjing Tech University, Nanjing 211816, China

^{*} Corresponding author: Hai Fang, College of Civil Engineering, Nanjing Tech University, Nanjing 211816, China, e-mail: fanghainjut@163.com

numerous investigations have demonstrated that the fiber winding angle significantly influences the bending performance of the piles [25–27].

In recent years, there has been increasing research interest in the development of composite structures incorporating FRP to enhance energy absorption capabilities [28-31]. Although experimental tests are straightforward and give good impact load measurements, they are usually costly, time-consuming, and sometimes impractical to perform. The finite element (FE) method is an alternative way to study the vessel-pier impact problem. Feng [32] and Wang and Zhang [33] conducted simulations of the impact process by establishing a vehicle-collision avoidance devicebridge FE model and found that it is necessary to choose the appropriate stiffness of the collision avoidance device. A large number of experimental studies and FE analyses showed that the composite collision avoidance system can significantly cut down the impact force, prolong the impact duration between the ship and the collision avoidance system, and mitigate the damage to the ship [34-36]. Wang et al. [37] studied a flexible guided anti-collision device and established FE models to simulate the impact process of a ship collision. The results showed that the anti-collision can significantly reduce impact force. Han et al. [38] proposed an innovative composite bumper device for bridge pier protection against ship collisions and found that the composite anti-collision has good energy absorption. Yan et al. [39] conducted a simulation of a box-soft anti-collision by using ANSYS/LS-DYNA FE and indicated that the anti-collision facilities' deformation energy absorption accounts for more than 70% of the total energy. However, most of the anti-collision facilities are in direct contact with the bridge, and the force generated by the impact will still be directly transmitted to the bridge, which is not conducive to bridge protection.

In this article, the installation of GFRP fender piles around the bridge pier for protection is shown in Figure 1, and the influence of different fiber winding angles on the

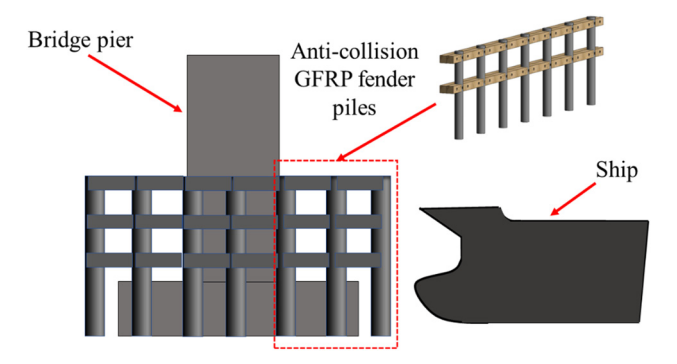


Figure 1: Installation of GFRP fender piles.

flexural performance of the pile is investigated. Bending tests and FE simulation were conducted to analyze the load—displacement relationship and damage process of the specimen, and the mechanical properties and damage modes of the specimen were compared and studied to investigate the effect of different fiber winding angles on the flexural performance of the GFRP pile. In addition, in this article, a numerical simulation of a ship impact on GFRP fender piles set up for the Nanjing Xiaoqiao Bridge was carried out using ANSYS/LS-DYNA FE analysis software, which aims to study the bending energy absorption performance of fender piles and provide valuable references for engineering applications.

2 Experimental section

2.1 Specimen description

The diameter of the GFRP pile specimens is 300 mm. To prevent the two ends from slipping during the test due to the large bending deformation, the total length of the specimens is 2,800 mm. The volume fraction of the GFRP is obtained as 70%. The specific dimensions of the test specimens are shown in Table 1. Label the 45° and 75° piles tested in the four-point bending test as F-D320-45 and F-D320-75. Label the 45° and 75° piles tested in the threepoint bending test as T-D320-45 and T-D320-75. The material properties of each GFRP have been tested and evaluated in the experimental program. The tensile tests were performed according to ASTM D3039/D3039M-14 [40], the dimensions of the five tensile specimens were $250 \times 25 \times 5$ mm³, and the tensile rate was 2 mm·min⁻¹. The shear tests were performed according to ASTM D3518/D3518M-94 [41], the dimensions of the five tensile specimens were $250 \times 25 \times 5$ mm³, and the tensile rate was 2 mm·min⁻¹. The compression tests were performed according to ASTM D3410/D3410M-16 [42], the dimensions of the five compression specimens were 150 \times $25 \times 5 \,\mathrm{mm}^3$, and the compression rate was $1 \,\mathrm{mm} \cdot \mathrm{min}^{-1}$. The details of the properties are provided in Table 2.

Table 1: The specimens of GFRP piles

Specimen number		Diagram	Winding angle (°)	Thickness (mm)
F-D320-45	T-D320-45		±45	10
F-D320-75	T-D320-75		±75	10

Table 2: The parameters of GFRP

Properties	(±45°)	(± 75°)
Modulus in longitudinal direction (GPa)	25.2	48.69
Modulus in transverse direction (GPa)	25.2	4.44
Shear modulus (GPa)	5.3	2.5
Longitudinal tensile strength (MPa)	185.2	305.2
Transverse tensile strength (MPa)	185.2	22
Longitudinal compressive strength (MPa)	180.3	265.6
Transverse compressive strength (MPa)	180.3	71.2
Shear strength (MPa)	20	15
Poisson's ratio (v_{12} , v_{21})	0.3	0.3

2.2 Experimental design

The microcomputer-controlled electronic universal testing machine was used for the four-point bending test. According to the ASTM D6272 [43,44] standard, the distance b between two loading points was set to 800 mm, the distance a between a side loading point and the support was set to 400 mm, and the distance L between two supports was set to 1,600 mm for the test, as shown in Figure 2.

The test was controlled with a loading speed of 2 mm·min⁻¹, and the loading mode was continuous loading. The strain gauges

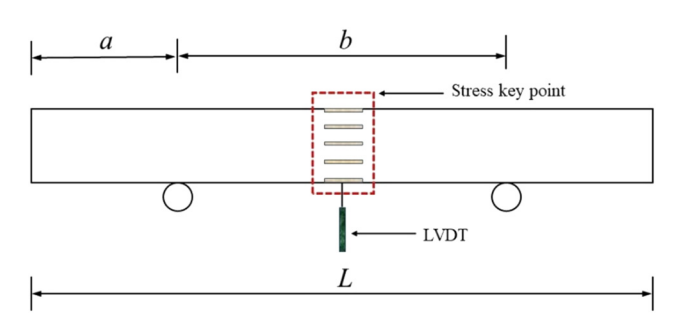


Figure 2: Technical illustration of the bending test.

were arranged at 45° intervals in the ring direction in the span of the specimen, and the axial and annular strains were collected, respectively, as shown in Figure 3(a). The displacement δ , load F, and strain ε were collected during the test loading process, and the final damage form was judged. The schematic diagram of the four-point bending test is shown in Figure 3(b).

The loading head arrangement used in the three-point bending test is shown in Figure 4, with strain gauges arranged at 45° intervals in the annular direction across the specimen to collect axial and annular strains, respectively. The bow of a ship is simulated by the U-shaped loading head. The distance between the loading point and one side of the support was 800 mm, and the loading speed control and

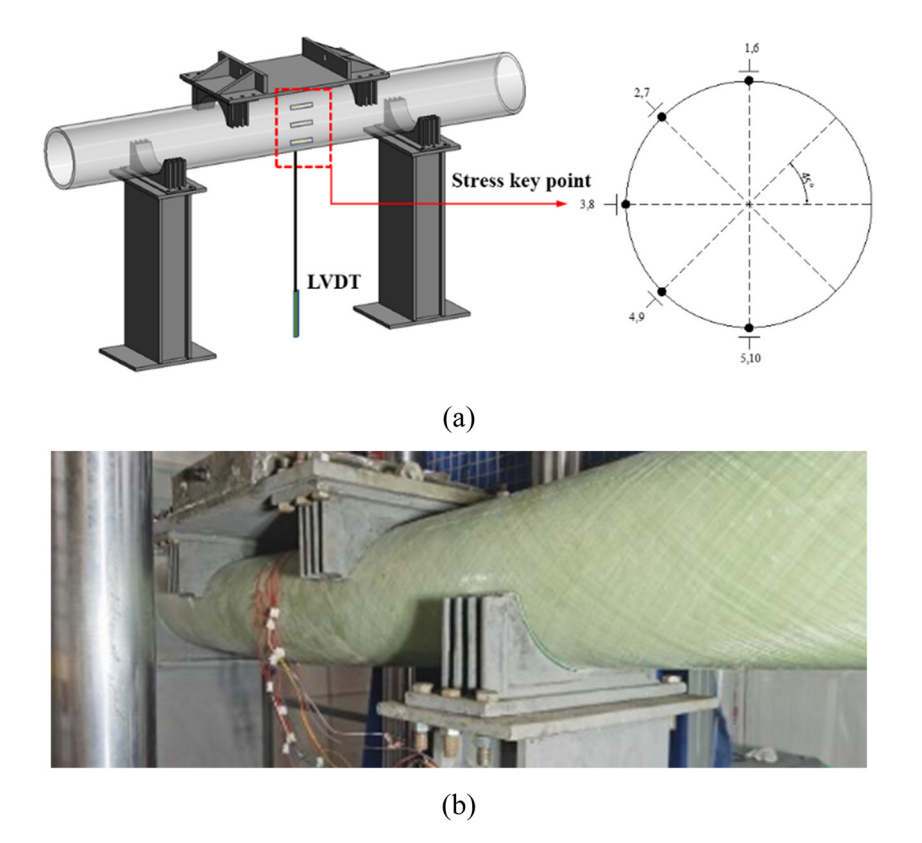


Figure 3: Instrumentation and test setup for four-point bending test: (a) strain gauge arrangement diagram and (b) four-point bending test machine.

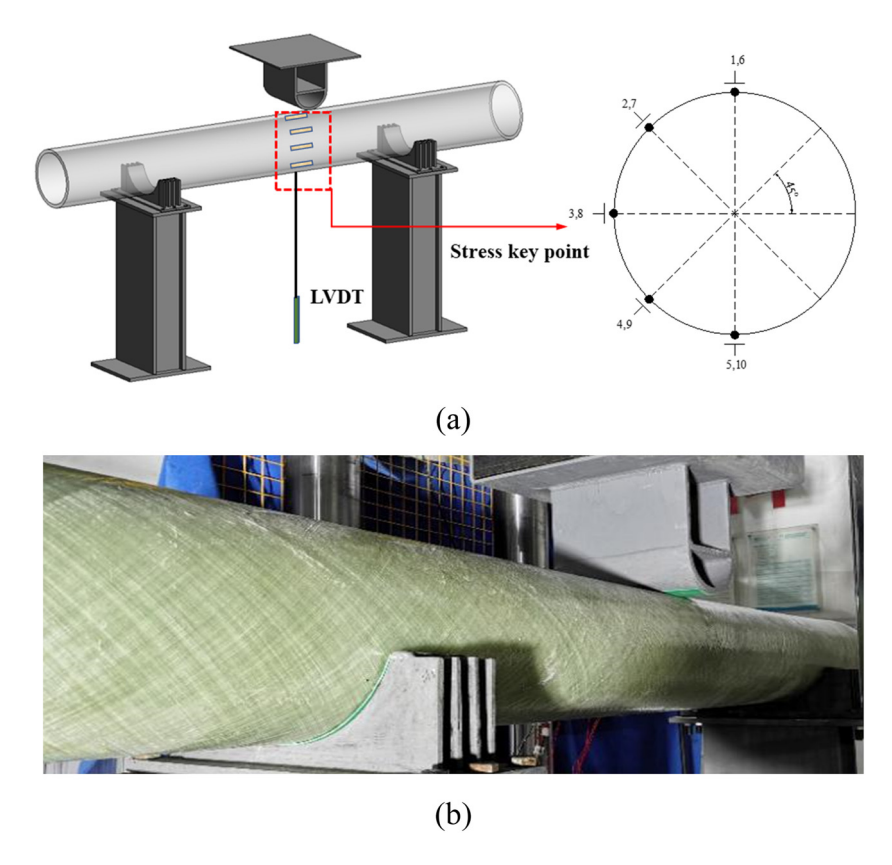


Figure 4: Instrumentation and test setup for three-point bending test: (a) strain gauge arrangement diagram and (b) three-point bending test machine.

loading method used in the three-point bending test were identical to those used in the four-point bending test.

3 Experimental assessment

3.1 Experimental process and results

3.1.1 Four-point bending test

The procedure and results of the four-point bending test conducted on the F-D320-45 specimens are shown in Figure 5. At the initial stage of the test, the specimen produced a slight ringing sound with no significant observations. With an increase in load, the upper fiber paving layer experiences local buckling. As the load continued to increase, no significant changes were observed. Despite the load increment, no substantial changes were observed. At higher loads, the specimen produced a loud noise but remained undamaged, and the top fiber surface continued to deform under tension. Although there were no significant load changes, the specimen displayed good ductility performance. The test progressed,

and noticeable bending of the specimen became evident, accompanied by a continuous zipping sound. At the peak load of 53 kN, a crushing sound was heard from the upper surface of the specimen, and the load rapidly dropped. Throughout the test, no significant load changes were observed, and damage was observed on the top surface of the specimen, while the bottom surface remained unaffected. As the load continued to increase, another sudden drop in load occurred. The test was stopped once the load reached the limit state. During unloading, the specimen partially rebounded, and the lower surface fibers returned to their initial position.

The four-point bending test procedure and results of the F-D320-75 specimen are shown in Figure 6. Initially, during the test, the specimen emitted a sound indicating fiber breakage, but no significant test results were observed. However, at a load of 18 kN, visible cracks appeared in the specimen, accompanied by a loud noise, and resulted in a rapid drop in load. Even when the loading was continued, the crack at the span widened continuously, producing a tearing sound. Upon unloading, the specimen returned to its original state, but the crack at the mid-span position remained open.

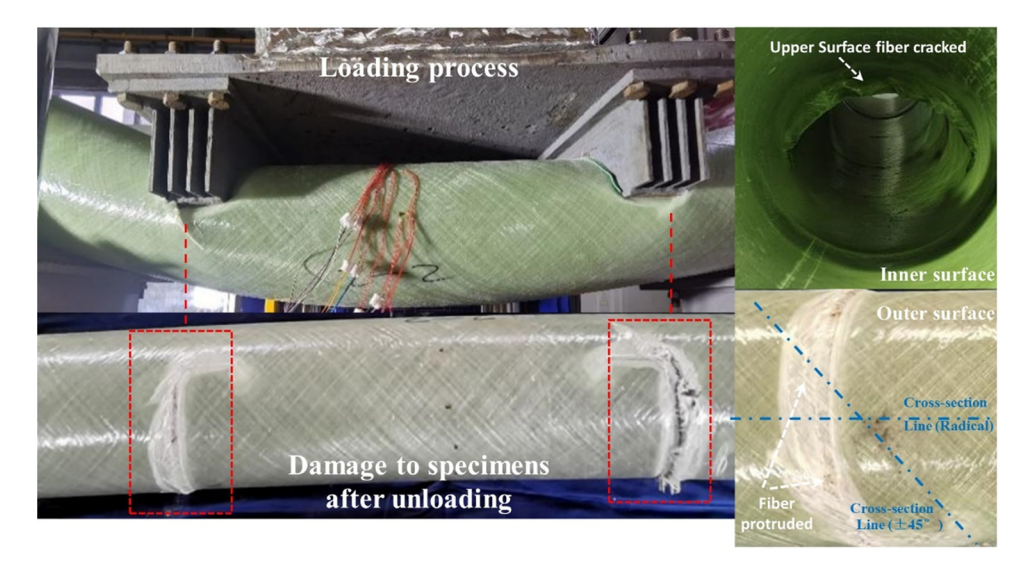


Figure 5: Damage details of specimen F-D320-45.

3.1.2 Three-point bending test

The procedure and results of the three-point bending test conducted on the T-D320-45 specimen are presented in Figure 7. Initially, at the start of the test, the top surface of the T-D320-45 specimen fractured upon contact with the loading head, resulting in a faint sound. When the load reached 31 kN, cracks appeared on the upper surface of the specimen, accompanied by the sound of fiber breakage. With further load increments, the cracks propagated axially, and the lower surface of the specimen exhibited significant buckling without losing its load-bearing capacity. The specimen reached its peak load at 41 kN. Subsequently,

as the test continued until its completion, no significant changes were observed in the specimen. During the unloading process, the specimen displayed a noticeable rebound, with the lower surface fibers returning to their original state.

The test procedure and results of the T-D320-75 specimen are shown in Figure 8(a) and (b) Initially, at the beginning of the test, the top surface of the specimen in contact with the loading head fractured, producing a slight sound. As the loading continued, the specimen demonstrated generalized bending behavior. Upon reaching a load of 32 kN, two symmetrical cracks emerged on the underside of the T-D320-75 specimen. With further load

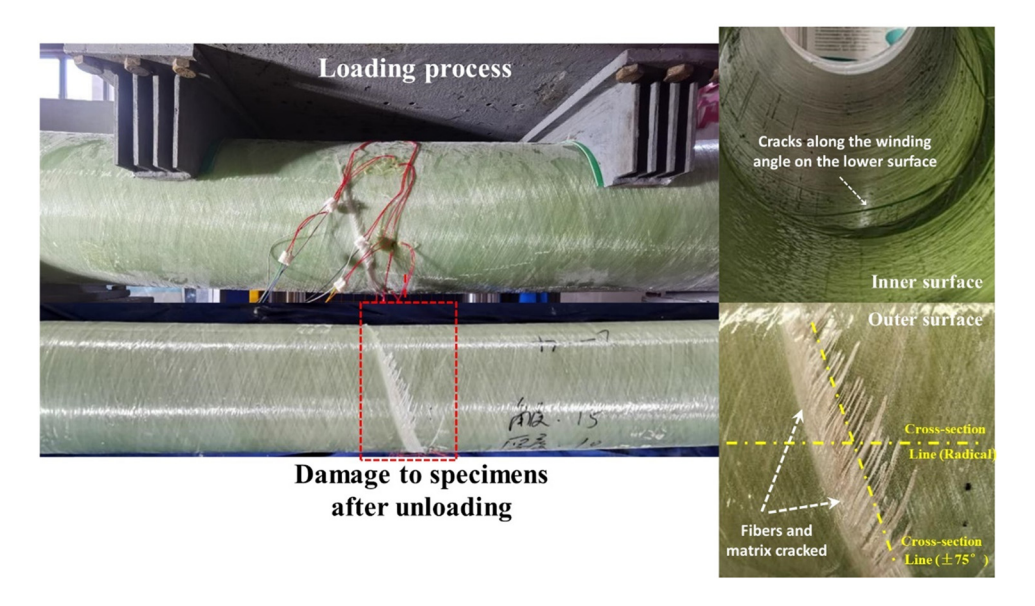


Figure 6: Damage details of specimen F-D320-75.

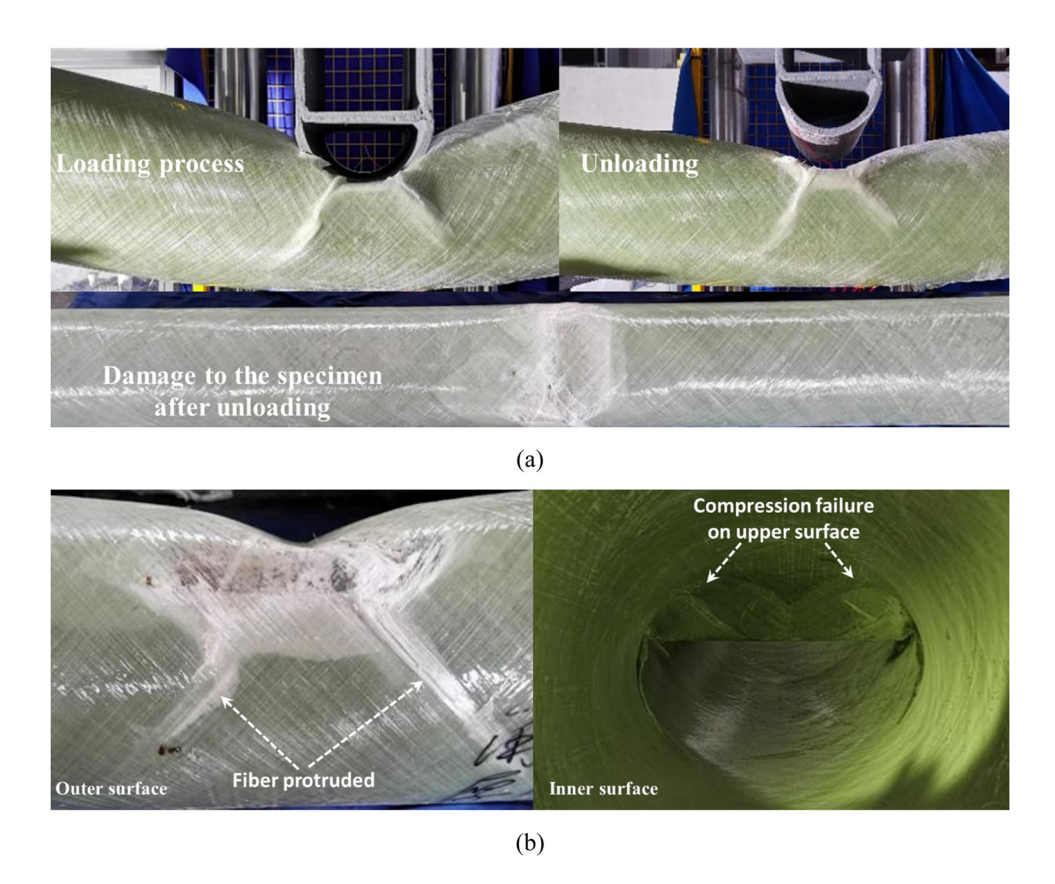


Figure 7: Three-point bending test result of the specimen T-D320-45: (a) process of test and (b) damage to the specimen.

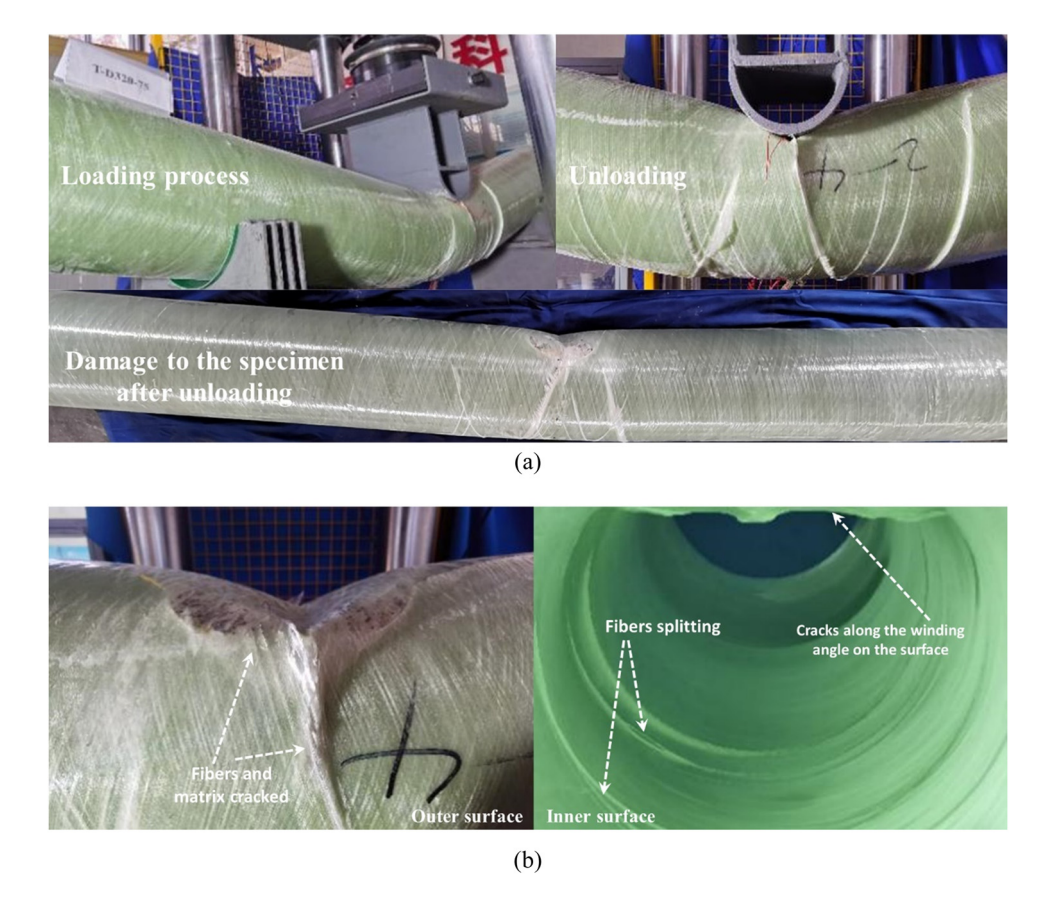


Figure 8: Three-point bending test result of the specimen T-D320-75: (a) process of test and (b) damage to the specimen.

increments, the specimen emitted sounds indicating fiber breakage, and the cracks propagated in the direction of fiber winding while new cracks appeared. At the peak load of 35 kN, the specimen exhibited visible bending. The load progressively decreased until the test concluded, while the cracking within the specimen increased significantly. During the unloading stage, the specimen displayed a slight rebound, accompanied by a faint sound.

3.2 Load-displacement curve

A comparison of the load–displacement curves for the four-point bend specimen is shown in Figure 9. The $\pm 45^{\circ}$ specimen, as depicted in the figure, can be roughly divided into three sections: the rising section, the falling section, and the yielding section. Initially, the load of the specimen increases linearly with displacement. Upon reaching the ultimate load, the upper surface of the $\pm 45^{\circ}$ specimen experiences destruction, causing the curve to enter the falling segment. Despite the ongoing bending of the specimen, the curve eventually enters the yielding segment, demonstrating good ductility. On the other hand, the $\pm 75^{\circ}$ specimen exhibits a linear increase in the curve during the elastic phase. However, when the peak load is attained, the curve rapidly declines due to the poor bending performance resulting from the distribution of fibers along the ring.

A comparison of the load—displacement curves of threepoint bending specimens is shown in Figure 10. The T-D320-75 specimen exhibits inferior flexural properties compared to the T-D320-45 specimen due to its larger slope during the

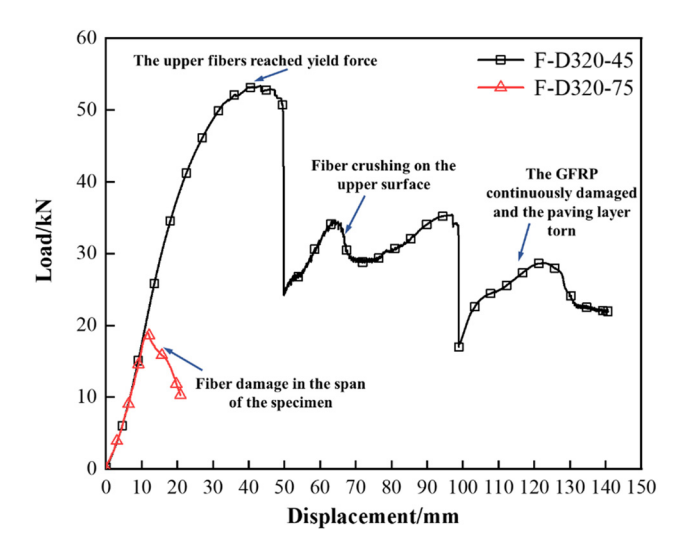


Figure 9: Load–displacement curve of specimens F-D320-45 and F-D320-75.

linearly increasing phase. In addition, the T-D320-45 specimen displays a short yielding plateau after reaching the ultimate load, whereas the T-D320-75 specimen lacks an obvious yielding plateau.

The bending moment will be determined by the load since the support distance is a fixed value. As shown in Figures 9 and 10, the maximum bending moment by F-D320-45 is greater than that of F-D320-75. Upon reaching the ultimate load, specimens of $\pm 45^{\circ}$ did not show brittle damage. Therefore, the ductility of the specimens with 45° winding angle was better than that of the 75° winding angle. The F-D320-45, F-D320-75, T-D320-45, and T-D320-75 specimens reach the yielding stage at compressions of 50, 14, 70, and 100 mm, respectively. By increasing the winding angle, the yielding stage can be advanced, and the damage mode of the specimens can be altered. The winding angle has a significant influence on the elongation of the specimens, with the $\pm 75^{\circ}$ specimens exhibiting poorer elongation compared to the $\pm 45^{\circ}$ specimens.

3.3 Comparison of bending test

To evaluate the flexural properties of GFRP piles, load—displacement curves from four- and three-point bending tests were compared, as shown in Figure 11.

The comparison of ultimate load capacity between bending tests is shown in Table 3. In the four-point bend test, the initial stiffness of the specimens is higher compared to the three-point bend test. This increase in stiffness

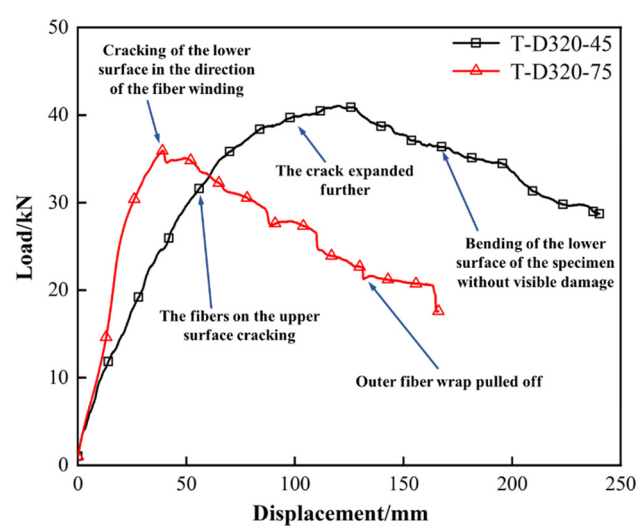
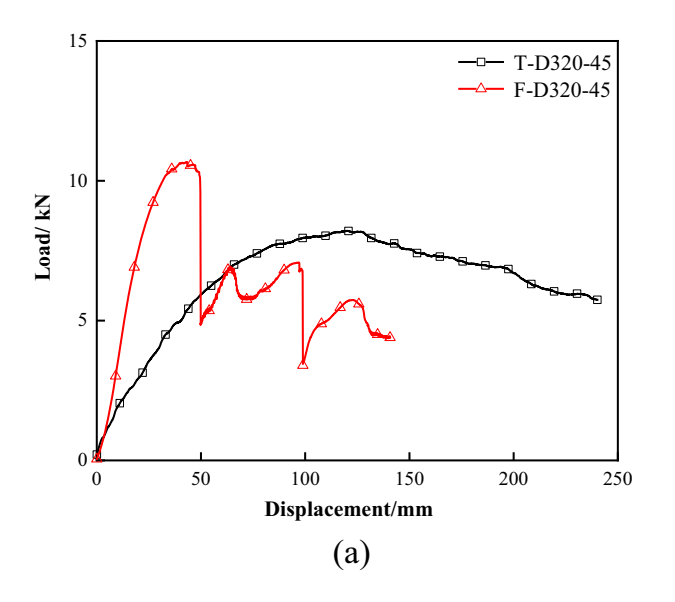


Figure 10: Load–displacement curve of the specimen T-D320-45 and T-D320-75



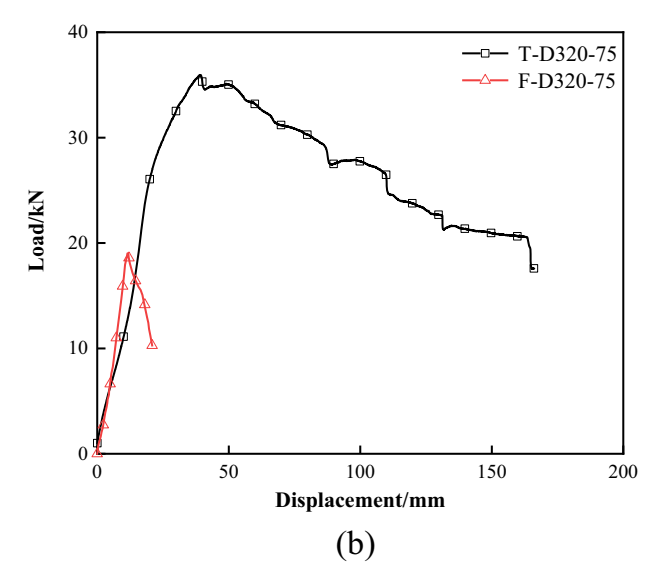


Figure 11: Comparison of load–displacement curve bending test results: (a) comparison of 45° winding angle bending test and (b) comparison of 75° winding angle bending test.

is due to the elimination of shear forces in the four-point bend configuration, resulting in higher initial flexural strength. Among the specimens with ±45° wraps, slightly higher ultimate strength is observed in the four-point bend test compared to the three-point bend test. However, the enhanced ductility observed in the ±45° specimens under three-point bending, characterized by a more prominent yield plateau, is less evident in the four-point bending tests. The loads drop suddenly around 50 mm in the four-point bend test, diminishing the observable yield plateau. Contrary to the ±45° specimens, the T-D320-75 and F-D320-75 samples exhibit a decline in ultimate bearing capacity under both three- and four-point bending. The ±75° winding angle is susceptible to shear damage, resulting in weak mid-span bending capacity and making it unsuitable for bearing larger four-point bending loads. At the initial stage of testing, a mid-span fracture occurs, leading to a continuous decrease in bearing capacity. While the ±75° winding angle can withstand a certain amount of shear force, it is important to avoid four-point bending damage for specimens

wound at $\pm 75^{\circ}$ to prevent sudden failure. When shear force and bending moment are applied simultaneously, the $\pm 75^{\circ}$ specimens demonstrate slightly better ductility and exhibit a more pronounced yield plateau. Therefore, it is recommended to avoid subjecting $\pm 75^{\circ}$ specimens to four-point bending, as their ductility is enhanced when exposed to shear force and bending moment together compared to bending moment alone.

During the test, the F-D320-45 specimen and T-D320-45 were exposed to pressure on the upper surface and tension on the lower surface. The upper part was compressed, inducing compressive stress. When the compressive stress exceeded the tensile strength of the resin, it led to cracking. Likewise, when the compressive stress exceeded the tensile strength of the fiber, circumferential cracking occurred along the winding angle of the fiber, which gradually expanded. The bottom surface was under tension; with the increase of tensile stress, the bottom fiber did not reach the ultimate tensile strength, and the fiber protrusion did not occur during the circumferential cracking. During the

Table 3: Comparison of bending test results

Specimen	Ultimate bearing capacity (kN)	Yield platform	Comparison of ultimate bearing capacity (%)	Load drop
T-D320-45	41.06	Yes	+29.93	No
F-D320-45	53.35	Yes		Yes
T-D320-75	35.95	Yes	-49.40	No
F-D320-75	18.20	No		Yes

Note: The contrast column shows the ultimate bearing capacity change of three-point bending test compared to flexural shear.

Table 4: Comparison of failure mode in four-point bending test

Specimen	Failur	e diagram	Failure modes
	External	Inside	•
F-D320-45	in Secretary		Local compression failure
F-D320-75			Monolithic shear failure

test, the specimen showed localized crushing damage, and no reduction in bending damage was observed after reaching the ultimate load.

The damage patterns of the F-D320-75 and T-D320-75 specimens were significantly different from the ±45° specimens. As the load continued, the lower surface of the

specimen flexed, producing several apparent cracks along the winding angle, and significant shear damage occurred. It is apparent that the interior of the specimen between the extrusion folds is subjected to different fiber layups, including the fiber layup and the peeling of the winding pile, as shown in Tables 4 and 5.

Table 5: Comparison of failure mode in three-point bending test

Specimen		Failure modes	
	External	Inside	
T-D320-45			Local compression failure
T-D320-75			Monolithic shear failure



Figure 12: The diagram of vertical impact test and FE: (a) FE models and (b) vertical impact test.

4 FE analysis

4.1 Validation of FE models

4.1.1 Modeling details

The composite fender piles were modeled and simulated using the FE software ANSYS/LS-DYNA. SHELL163 element was used to simulate the GFRP specimens with different winding angles. The thickness of different GFRPs was defined by setting real constant, and SOLID164 element was used to simulate test loading rigid head and backing rigid plate (Figure 12).

The loading rigid head and backing rigid plates used *MAT_003 (MAT_PLASTIC_KINEMATIC) and the composite fender piles used *MAT_054-055 (*MAT_ENHANCED_COMPOSITE_DAMAGE) as the material model for FE analysis, and the relevant parameters are given in Table 6. As shown

Table 6: The material parameters of vertical impact FE model

*MAT_003		*MAT_054-055	
ρ (kg·m ⁻³)	7,850	ρ (kg·m ⁻³)	2,030
<i>E</i> (GPa)	200	E_1 (GPa)	270.58
		E_2 (GPa)	118.43
V	0.27	V	0.09
G (MPa)	310	G_1 (MPa)	7,000
		G_2 (MPa)	4,000
β	0	X_{t}	826
С	40	X_{c}	700
Ρ	5	Y_{t}	88
ε	0.35	Y _c	142

Note: ρ is density; E, E, and E are elastic modulus; V is Poisson's ratio; G is yield stress; G and G are shear modulus; X1 and X2 are tensile strength; Y4 and Y5 are compressive strength; G6 is strain rate parameter for Cowper–Symonds strain rate model; G7 is strain rate parameter for Cowper–Symonds strain rate model; G8 is failure strain for eroding elements.

in Figure 13, the composite layers used *Part_Composite as the material model and repeat the operation for all layers.

4.1.2 Loading and boundary conditions

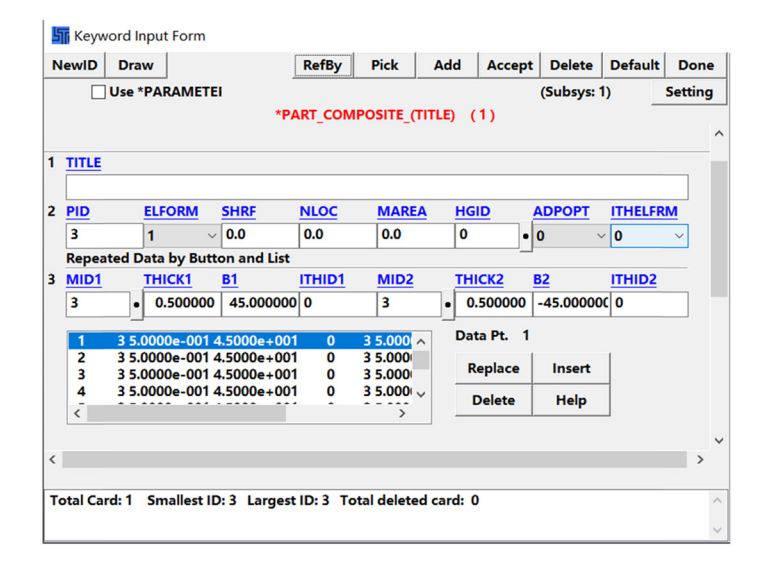
The FE model boundary control condition is consistent with the experimental loading control condition. The bottom rigid plate was fixed, and the loading head was loaded by the method of specifying loads. The contact algorithm *CONTACT_AUTOMATIC_ SURFACE_TO_SURFACE was used between the loading head and the composite specimen, and the static and dynamic friction coefficients were set to 0.1. The contact algorithm *TIED_ SURFACE_TO_SURFACE was used between the bottom rigid plate and the composite specimen.

The impact head is the same size as the bending test U-head, which is connected to the drop hammer. The displacement gauge is arranged directly below the span. The arrangement of strain gauges is consistent with the bending test. The test adopts a vertical impact system, the impact force is measured by the force sensor, and the output signal is automatically recorded. The distance between the loading head and the soft body layer was set at 2 m for vertical impact.

4.1.3 Validation of force-time curve

Under dynamic loading, the specimen has been severely deformed and lost its bearing capacity, which is particularly obvious for a 75° specimen. In the vertical impact test, the damage mode of the 45° pipe was local failure damage, while the 75° winding members had a mid-span shear damage.

Figure 14 shows the deformation diagram of the specimens obtained by FE numerical simulation coincides with the experimental compression deformation results. The bending failure of specimens is the same as the experimental result. Figure 15 draws force—time curves of numerical simulations and experimental data.



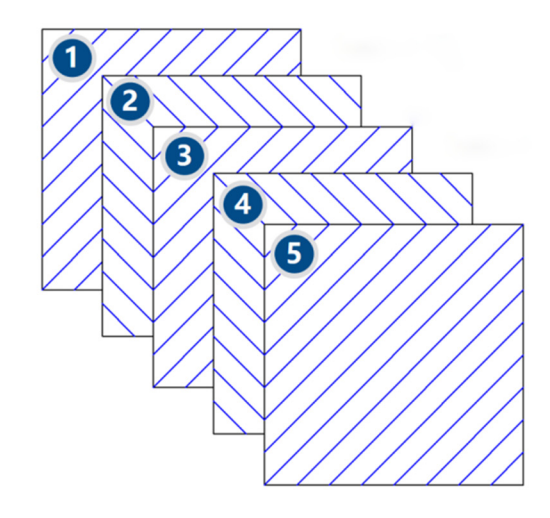


Figure 13: Diagram of ±45° composite laminates.

The numerical result of the impact force of the specimens is slightly larger than the experimental result. During the impact process, the support will have a certain amount of slip, whereas the support is defined as a rigid body and constrained in the FE simulation, which leads to a certain amount of difference between the test curve and the FE curve. A comparison of the results of the test and FE simulation for specimens is shown in Table 7. The error is within tolerance and the FE data can be considered reliable.

4.2 FE analysis of composite fender piles

The Nanjing Xiaoqiao bridge located in Pukou District, Nanjing City, carries the high risk of ship—bridge collisions, as shown in Figure 16. Therefore, it is crucial to install anticollision facilities for the bridge piers against a potential ship—bridge collision. The schematic diagram of the bridge

is shown in Figure 17(a), and the structural diagram of the piers is shown in Figure 17(b)–(d). The pile–soil relative position is shown in Figure 17(e).

4.2.1 Numerical model

In this article, we developed a detailed numerical model of ship-pier collision using the ANSYS/LS-DYNA software

Table 7: Comparison of the results of the test and FEM for specimens

Specimen	Impact	Impact velocity (m·s ⁻¹)	Impact force (kN)		
	height (m)		Test value	FE value	Error (%)
D320-45 D320-75	2 2	6.32 6.32	49.26 43.77	51.97 49.09	5.50 12.2

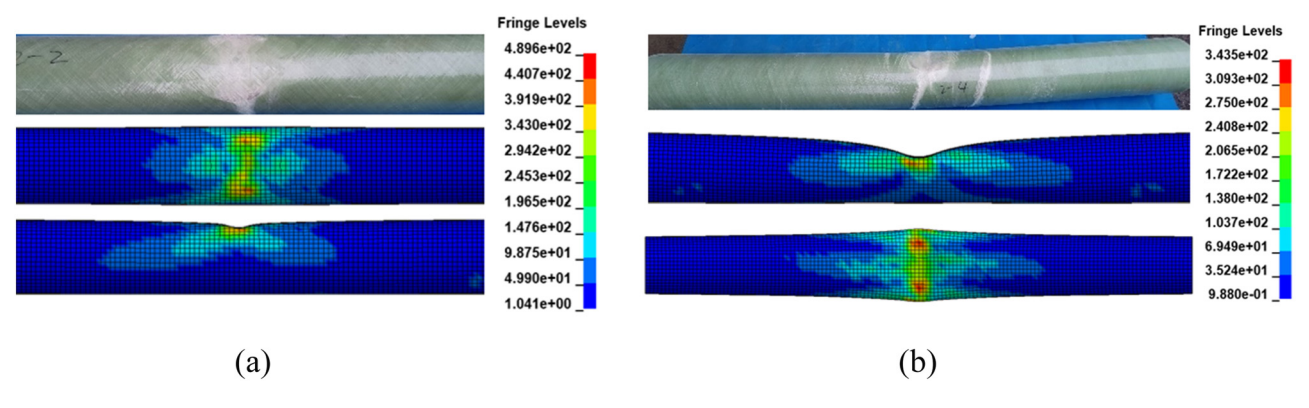


Figure 14: The deformation diagram of the specimens: (a) D320-45 specimen and (b) D320-75 specimen.

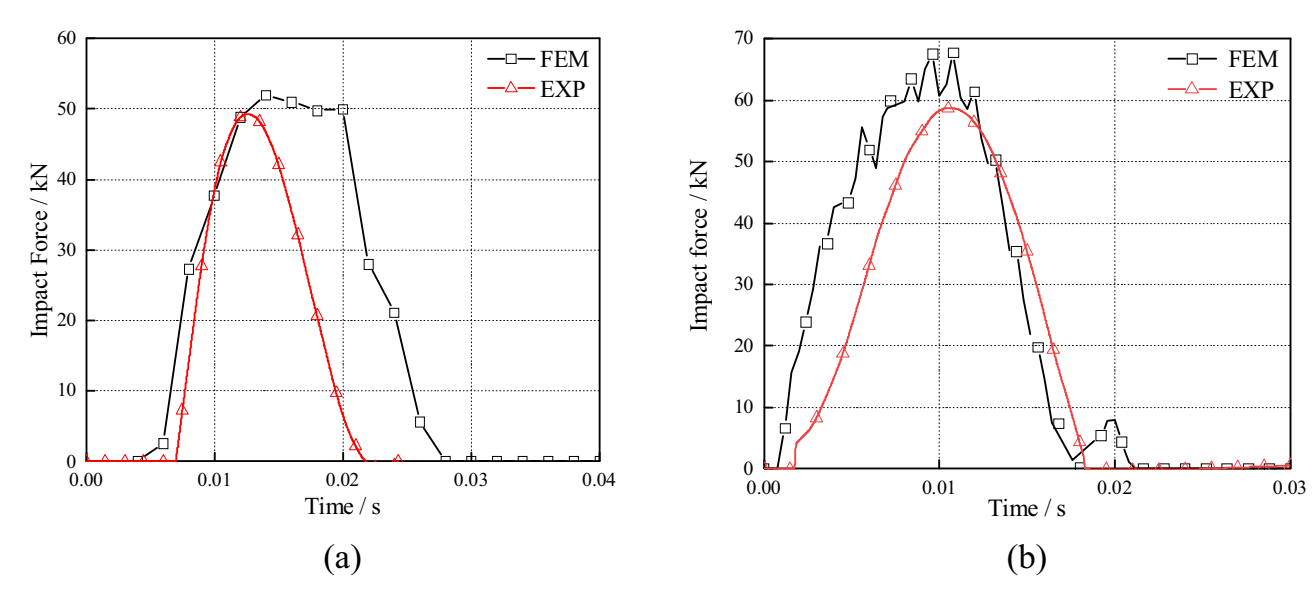


Figure 15: The force-time curves of numerical simulations and experimental data: (a) D320-45 specimen and (b) D320-75 specimen.

package. The computed results were analyzed using the post-processing software LS-PREPOST. The anti-collision design scheme incorporates the use of GFRP fender piles. To prevent the fender piles from shearing, it is coiled at ±45°. Each pile has a diameter of 30 cm and a total length of 12 m. The positioning of the bottom of the pile is determined based on soil quality and impact location, which is set at twice the distance from the mud line to the top of the pile. Based on the actual situation of the bridge area, three sides of frame piles are added to it, which are connected by two girders spaced at 1.5 m. The wall thickness is 0.15 m, and the pile spacing is 0.8 m with a net spacing of 0.5 m. The distance from the bridge pier is 1 m. A comparative

analysis of the energy consumption effects between GFRP collision piles and frame structures will be conducted. The plan view is shown in Figure 18.

According to the geological parameters of the site, the pile–soil interaction is considered in the way that the pile length was supposed to be four times the pile diameter below the mud line. An elastic material was applied to model the concrete pier, and its Young's modulus ratio and Poisson's ratio were 32.5 MPa and 0.2, respectively. For the FE modeling, the *MAT_Plastic_Kinematic model was used for the simulation of the ship's bow. The material parameters for the bow and fender piles were the same as in the previous section. According to the engineering practice, concrete was filled in piles.



Figure 16: Nanjing Xiaoqiao Bridge.

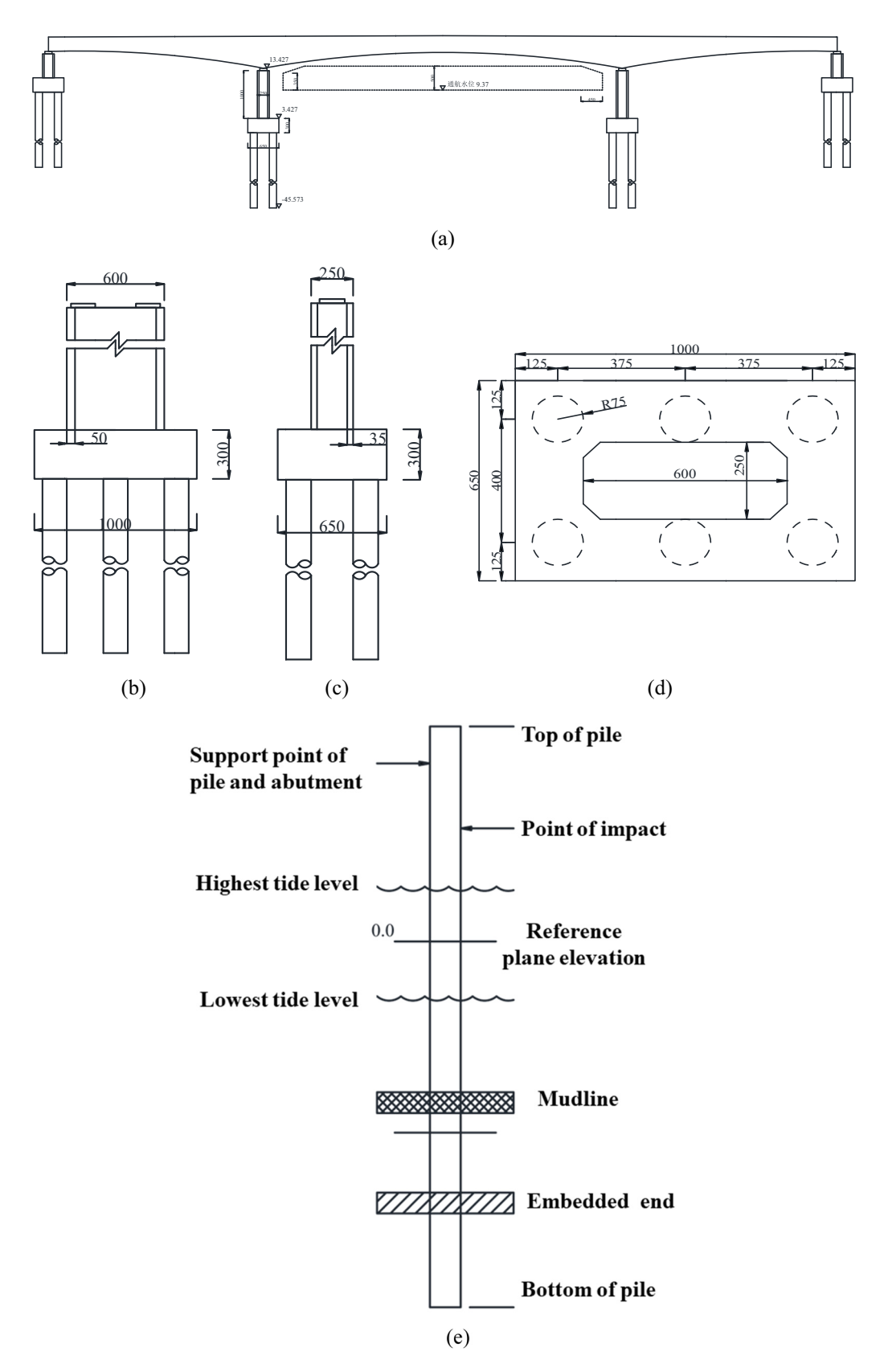


Figure 17: Pier structure diagram: (a) bridge layout, (b) elevation plan, (c) side view, (d) pier structure drawing, and (e) pile-soil relative position.

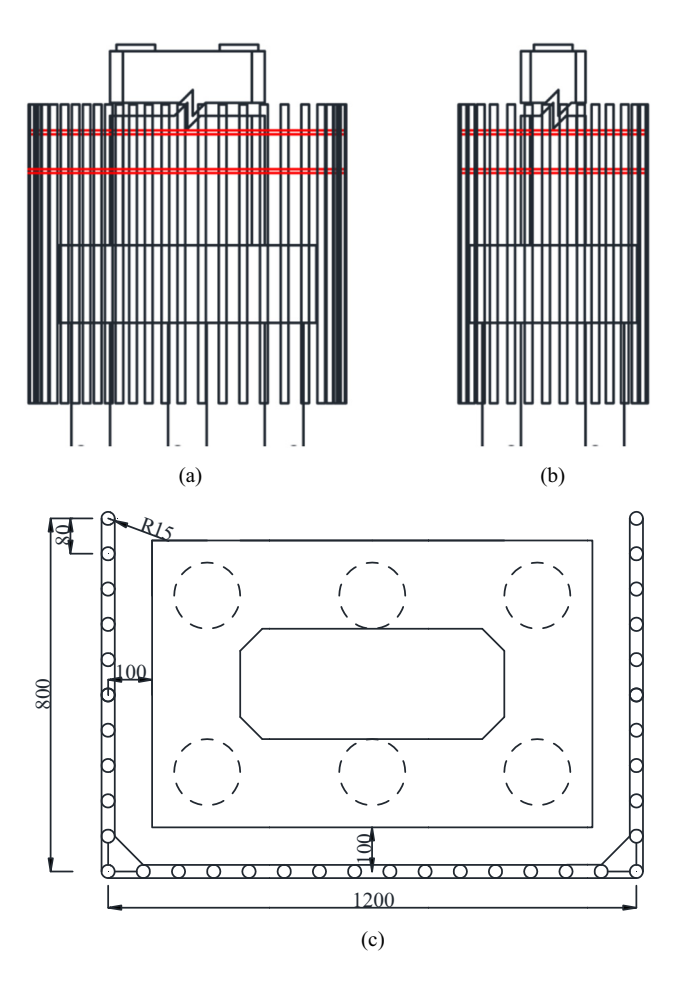


Figure 18: Protection replacement of fender piles: (a) fender elevation, (b) side view, and (c) plan view.

The contact algorithm CONTACT_AUTOMATIC_SURFACE_TO_SURFACE was defined for the bow and the fender piles, the bow and the bridge pier, and the fender piles and the bridge pier contact. The dynamic and static friction coefficients were set to be 0.2. The contact algorithm CONTACT_TIED_SHELL_EDGE_TO_SURFACE_OFFSET was defined for concrete and GFRP piles contact.

The FE modeling for the collision of the ship's bow with the pile and the pier is shown in Figure 19. The typical ship is 300 dead weight tonnage (DWT). For this study, the collision speed has been set at $4.1\,\mathrm{m\cdot s^{-1}}$ based on practical engineering considerations. The forward direction of the ship will be set as follows: one is perpendicular to the direction of bridge construction (head-on collision in *x*-direction) and the other is at an angle of 20° to the vertical line of the bridge pier.

4.2.2 Simulation results

Fender piles can efficiently prevent the bow of the ship from colliding with the bridge, ensuring that the bow only comes into contact with the fender piles. The vectorial decomposition of the peak impact force in the X and Y directions is shown in Figure 20 and Table 8. The duration of impact is 0.43 and 0.95 s, which represents an increase of 120.93% compared to the impact duration on the bridge pier. The deformation of the bow and distribution of stress can be shown in Figure 21. The results indicated that the

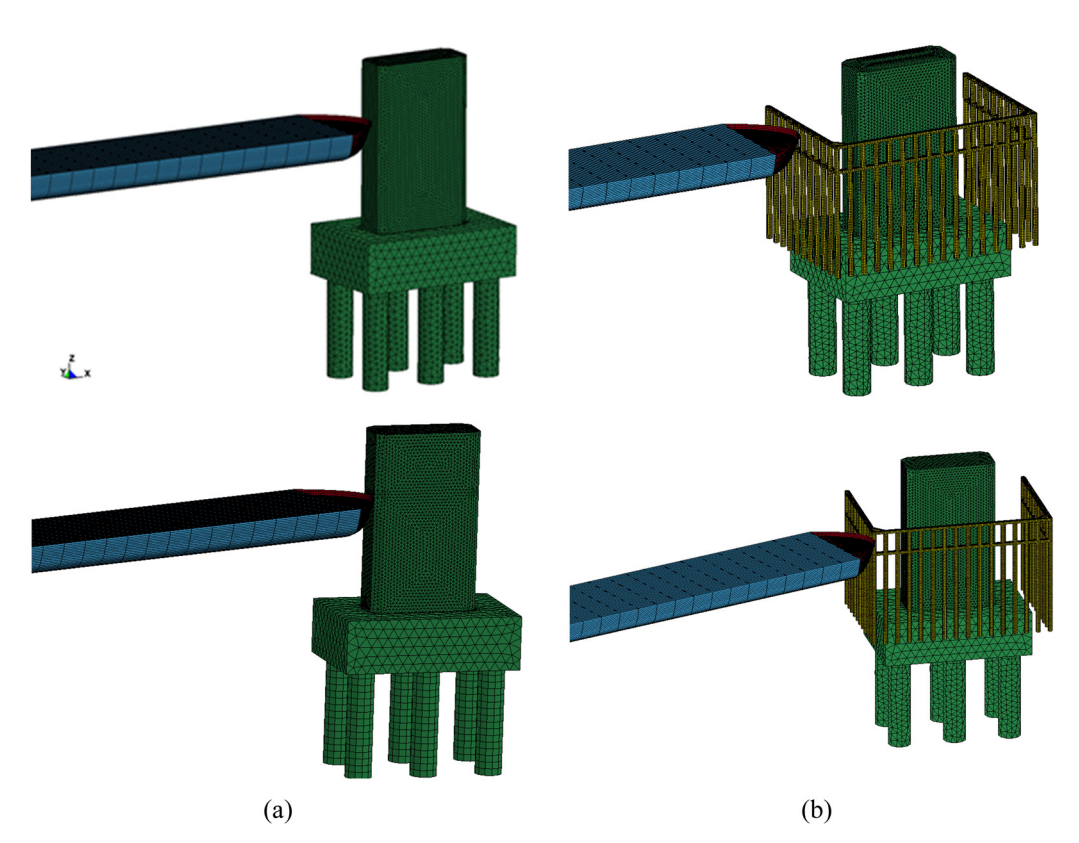


Figure 19: FE model: (a) ship-bridge collision and (b) ship collision with fender piles.

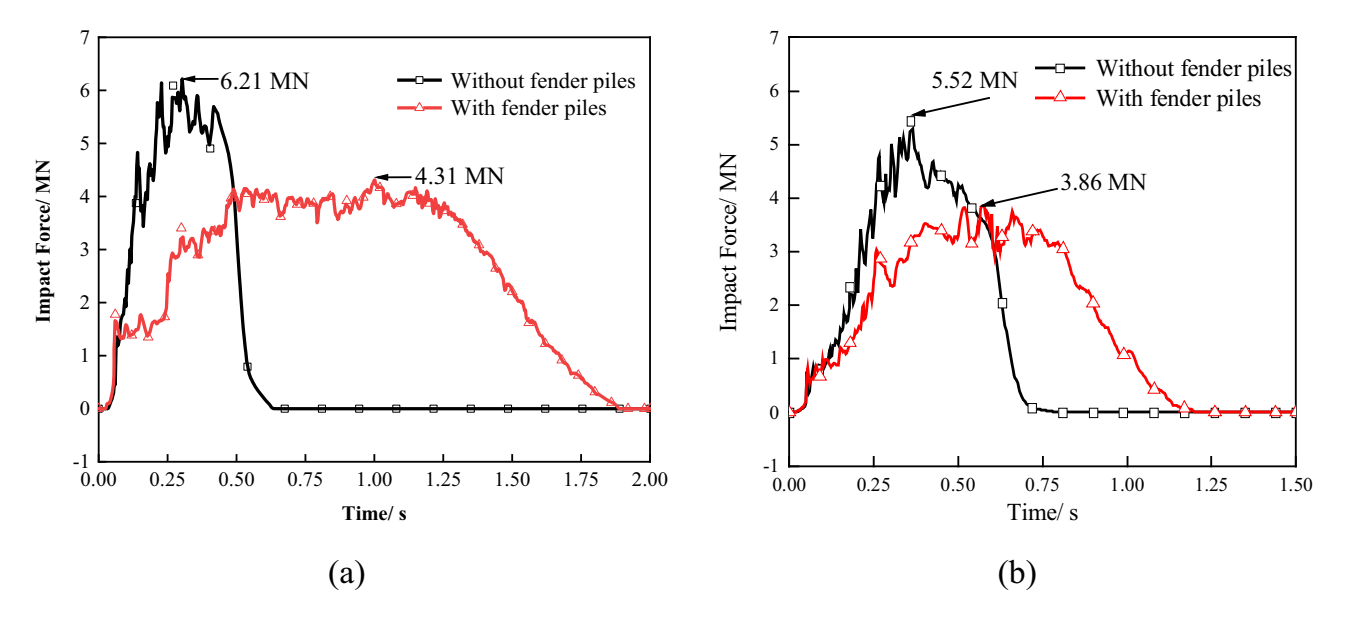


Figure 20: Comparison of time history curve of impact (cross bridge direction): (a) head-on collision and (b) 20° angle of impact.

Table 8: Comparison of ship impact force and duration

Bridge impact condition	Ship impact f	orce (MN)	Impact duration (s) Contra	
	Cross bridge direction	Bridging direction		
Head-on collision without fender piles	6.21	0.47	0.43	120.93
Head-on collision with fender piles	4.31	1.92	0.95	
20° angle collision without fender piles	5.52	2.23	0.57	24.56
20° angle collision with fender piles	3.86	1.53	0.71	

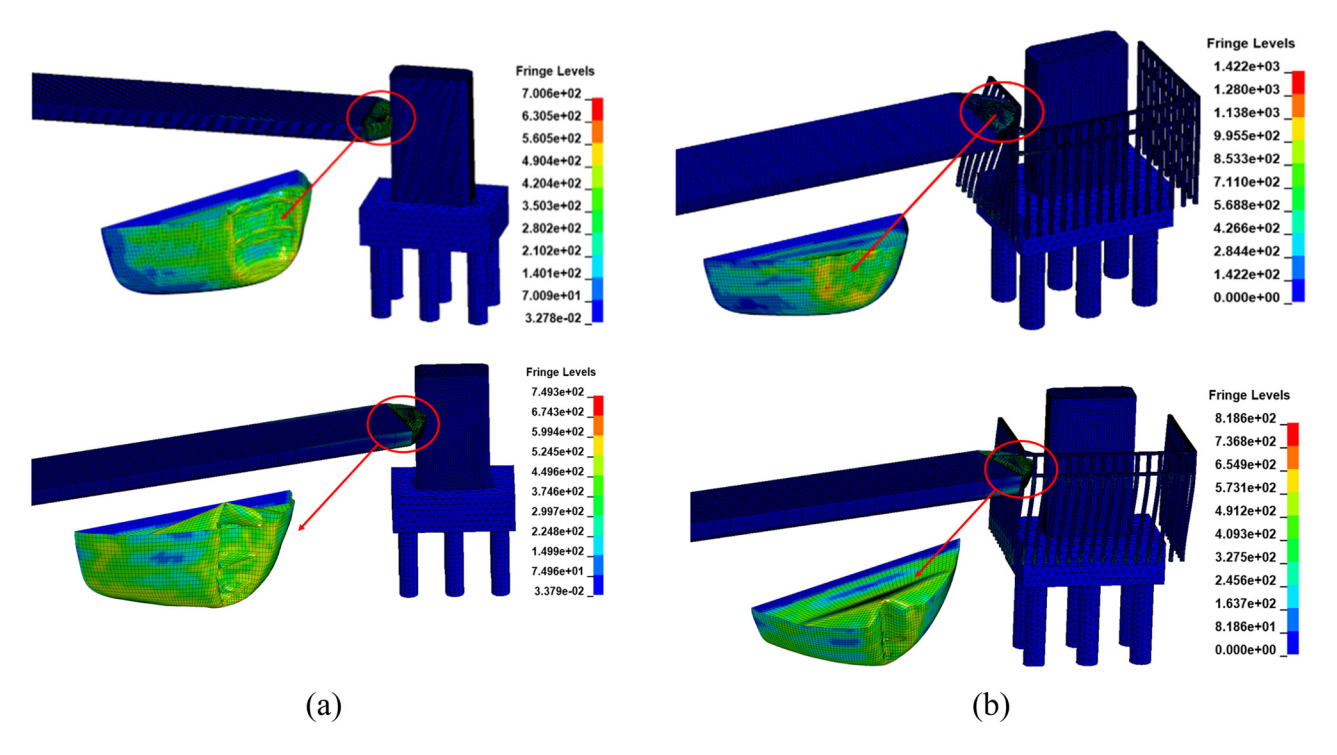


Figure 21: Deformation of the bow and distribution of stress: (a) ship-bridge collision and (b) ship collision with fender piles.

fender piles were effective in protecting both the ship and the bridge pier.

5 Conclusions

In this article, a type of fender pile made of windingformed GFRP is proposed and subjected to both threeand four-point bending tests. An FE model is established to simulate the vertical impact process to ensure its validation. Finally, an FE model for the simulation of the impact of ship collision is constructed to validate the effectiveness. The discussions and numerical analysis allow the following conclusions to be drawn:

- 1) The ±45° specimen demonstrates overall bending damage and exhibits good ductility, with compression on the upper surface and tension on the lower surface. In contrast, the ±75° specimen exhibits a wider fiber crack along the span and shows evidence of shear damage, resulting in weaker flexural performance compared to the ±45° specimen. The damage mode of the specimen significantly changes with an increase in the winding angle. Therefore, it is crucial to select the appropriate winding angle based on specific conditions in actual engineering applications to avoid shear damage.
- 2) The load–displacement curves of the four-point bending test and the three-point bending test exhibit different behaviors. Four-point bending should be avoided as much as possible as it reduces the ductility of the pile and results in sudden load drops. Therefore, 45° is chosen as the winding angle in this article.
- 3) The FE model on account of experimental material properties could well forecast the impact response. The GFRP fender piles installed on the pier of the Nanjing Xiaoqiao Bridge are simulated by the FE method. A comparative analysis of impact force and duration of impact between different conditions with and without fender piles.
- 4) The simulation results indicated that fender piles can effectively increase the impact time of ship-bridge collision and reduce the peak collision forces to increase the safety factor of the bridge piers, leading to a good effect in energy dissipation.

Acknowledgments: The research described herein was supported by the National Natural Science Foundation of China (Grant No. 52208252), Basic Research on Impact Energy Absorption Mechanism of Composite Soft Body System and Application to Bridge Ship Collision Prevention (Grant No.

52078248), Novel Fiber-reinforced Composite Structures for Marine Photovoltaics and Dynamic Mechanical Properties (Grant No. 52378241).

Funding information: The research described herein was supported by the National Natural Science Foundation of China (Grant No. 52208252), Basic Research on Impact Energy Absorption Mechanism of Composite Soft Body System and Application to Bridge Ship Collision Prevention (Grant No. 52078248).

Author contributions: C.W.S. proposed the concept and research method of composite fender piles, used ANSYS/LS-DYNA to conduct the numerical simulation, and wrote the manuscript. F.H. explained the professional terms and participated in the discussion of research methods. Z.L. analyzed the anti-collision facility and conducted the numerical simulation. Z.X.C. revised and edited the manuscript. Z.J.Y. participated in the discussion of the research methods. All authors have accepted responsibility for the entire content of this manuscript and approved its submission.

Conflict of interest: The authors state no conflict of interest.

Data availability statement: The datasets generated during and/or analyzed during the current study are available from the corresponding author on reasonable request.

References

- [1] Qiu, A., W. Lin, Y. Ma, C. B. Zhao, and Y. H. Tang. Novel material and structural design for large-scale marine protective devices. *Materials & Design*, Vol. 68, 2015, pp. 29–41.
- [2] Xing, L., Z. Feng, J. Bao, and S. Li. Facing opportunity and challenge of carbon fiber and polymer matrix composites industry development. *Acta Materiae Compositae Sinica*, Vol. 37, 2020, pp. 2700–2706.
- [3] Kang, L., K. Magoshi, H. B. Ge, and T. Nonaka. Accumulative response of large offshore steel bridge under severe earthquake and ship impact due to earthquake-induced tsunami flow. *Engineering Structures*, Vol. 134, 2017, pp. 190–204.
- [4] Guo, X., C. Zhang, and Z. Q. Chen. Dynamic performance and damage evaluation of a scoured double-pylon cable-stayed bridge under ship impact. *Engineering Structures*, Vol. 216, 2020, id. 110772.
- [5] Irhayyim, A., M. Gunaratne, and A. Fioklou. Assessment of scoured bridges subjected to ship impact. Structures, Vol. 36, 2022, pp. 635–649.
- [6] Fan, W., W. Guo, Y. Sun, B. S. Chen, and X. D. Shao. Experimental and numerical investigations of a novel steel-UHPFRC composite fender for bridge protection in vessel collisions. *Ocean Engineering*, Vol. 165, 2018, pp. 1–21.
- [7] Fan, W. and W. C. Yuan. Numerical simulation and analytical modeling of pile-supported structures subjected to ship collisions

- including soil-structure interaction. Ocean Engineering, Vol. 91, 2014, pp. 11-27.
- [8] Frketic, J., T. Dickens, and S. Ramakrishnan. Automated manufacturing and processing of fiber-reinforced polymer (FRP) composites: An additive review of contemporary and modern techniques for advanced materials manufacturing. Additive Manufacturing, Vol. 14, 2017, pp. 69-86.
- Ning, F. D., W. L. Cong, Z. L. E. Hu, and K. Huang. Additive manufacturing of thermoplastic matrix composites using fused deposition modeling: A comparison of two reinforcements. Journal of Composite Materials, Vol. 51, 2017, pp. 3733-3742.
- [10] Otoom, O. F., W. Lokuge, W. Karunasena, A. C. Manalo, T. Ozbakkaloglu, and D. Thambiratnam. Experimental and numerical evaluation of the compression behaviour of GFRP-wrapped infill materials. Case Studies in Construction Materials, Vol. 15, 2021, id. e00654.
- [11] Dorigato, A. and A. Pegoretti. Flexural and impact behaviour of carbon/basalt fibers hybrid laminates. Journal of Composite Materials, Vol. 48, 2014, pp. 1121-1130.
- [12] Zeng, J. J., Z. J. Duan, Y. C. Guo, Z. H. Xie, and L. J. Li. Novel fiberreinforced polymer cross wrapping strengthening technique: A comparative study. Advances in Structural Engineering, Vol. 23, 2020, pp. 979-996.
- [13] Cai, H., J. Wang, X. Zhao, and J. Wang. Study of bending properties of filament winding pipe. Fiber Reinforced Plastics/Composites, Vol. 8, 2013, pp. 31-34.
- [14] Vincent, T. and T. Ozbakkaloglu. Influence of fiber orientation and specimen end condition on axial' compressive behavior of FRPconfined concrete. Construction and Building Materials, Vol. 47, 2013, pp. 814-826.
- [15] Zhang, B., J. L. Zhao, T. Huang, N. Y. Zhang, Y. J. Zhang, and X. M. Hu. Effect of fiber angles on hybrid fiber-reinforced polymer-concrete-steel double-skin tubular columns under monotonic axial compression. Advances in Structural Engineering, Vol. 23, 2020, pp. 1487-1504.
- [16] Jin, Q., J. Wang, J. Y. Chen, and F. L. Bao. Axial compressive behavior and energy absorption of syntactic foam-filled GFRP tubes with lattice frame reinforcement. Composite Structures, Vol. 299, 2022, id. 116080.
- [17] Gemi, L., E. Madenci, Y. O. Özkiliç, S. Yazman, and A. Safonov. Effect of fiber wrapping on bending behavior of reinforced concrete filled pultruded GFRP composite hybrid beams. Polymers, Vol. 14, 2022, id. 3740.
- [18] Gemi, D. S., Ö. Sahin, and L. Gemi. Experimental investigation of axial compression behavior after low velocity impact of glass fiber reinforced filament wound pipes with different diameter. Composite Structures, Vol. 280, 2022, id. 114929.
- [19] Gemi, D. S., O. S. Sahin, and L. Gemi. Experimental investigation of the effect of diameter upon low velocity impact response of glass fiber reinforced composite pipes. Composite Structures, Vol. 275, 2021, id. 114428.
- [20] Gemi, L., E. Madenci, and Y. O. Özkiliç. Experimental, analytical and numerical investigation of pultruded GFRP composite beams infilled with hybrid FRP reinforced concrete. Engineering Structures, Vol. 244, 2021, id. 112790.
- [21] Gemi, L., U. Köklü, S. Yazman, and S. Morkavuk. The effects of stacking sequence on drilling machinability of filament wound hybrid composite pipes: Part-1 mechanical characterization and drilling tests. Composites Part B-Engineering, Vol. 186, 2020, id. 107787.

- [22] Gemi, L., S. Morkavuk, U. Köklü, and S. Yazman. The effects of stacking sequence on drilling machinability of filament wound hybrid composite pipes: Part-2 damage analysis and surface quality. Composite Structures, Vol. 235, 2020, id. 111737.
- Gemi, L., M. Kayrici, M. Uludag, D. S. Gemi, and Ö. Sahin. Experimental and statistical analysis of low velocity impact response of filament wound composite pipes. Composites Part B-Engineering, Vol. 149, 2018, pp. 38-48.
- [24] Gemi, L., M. A. Köroglu, and A. Ashour. Experimental study on compressive behavior and failure analysis of composite concrete confined by glass/epoxy ±55° filament wound pipes. Composite Structures, Vol. 187, 2018, pp. 157-168.
- [25] Su, W., X. Zhang, K. Wei, Z. Su, and D. Wang. Pre-stress dynamic performance during filament winding with tension. Acta Materiae Compositae Sinica, Vol. 36, 2019, pp. 1143-1150.
- [26] Azeem, M., H. H. Ya, M. A. Alam, M. Kumar, P. Stabla, M. Smolnicki, et al. Application of filament winding technology in composite pressure vessels and challenges: A review. Journal of Energy Storage, Vol. 49, 2022, id. 103468.
- [27] Farhangi, V. and M. Karakouzian. Effect of fiber reinforced polymer tubes filled with recycled materials and concrete on structural capacity of pile foundations. Applied Sciences-Basel, Vol. 10, 2020, id. 10051554.
- [28] Jiang, H., B. Geng, and X. Zhang. A new fender system for bridge pier protection against vessel collision. Journal of Vibration and Shock, Vol. 33, 2014, pp. 154-160.
- [29] Chen, W., B. Geng, R. Shen, and Z. Zheng. A functional study of rotary anti-ship-collision facility. Journal of Ship Mechanics, Vol. 24, 2020, pp. 525-535.
- [30] Zhang, Q. L., H. Fang, L. Zhu, J. Han, X. C. Zhang, X. L. Li, et al. Impact behavior of corrugated-core infilling foam sandwich composite structure. Case Studies in Construction Materials, Vol. 17, 2022, id. e01418.
- [31] Sun, S. Z., L. Chen, T. Liu, D. J. Zhou, and M. Q. Yue. Energy absorption performance of steel plate-polyurethane foam composite protective structures. Case Studies in Construction Materials, Vol. 17, 2022, id. e01496.
- [32] Feng, Q. On the performance of anti-collision steel box for largespan bridge and collision process analysis. Chinese Quarterly of Mechanics, Vol. 39, 2018, pp. 859-865.
- [33] Wang, X. and L. Zhang. Comparative analysis on performance of solid cylinder pier anti-collision devices. Journal of Highway and Transportation Research and Development, Vol. 39, 2022,
- [34] Fang, H., Y. F. Mao, W. Q. Liu, L. Zhu, and B. Zhang. Manufacturing and evaluation of large-scale composite bumper system for bridge pier protection against ship collision. Composite Structures, Vol. 158, 2016, pp. 187-198.
- [35] Wan, Y. L., L. Zhu, H. Fang, W. Q. Liu, and Y. F. Mao. Experimental testing and numerical simulations of ship impact on axially loaded reinforced concrete piers. International Journal of Impact Engineering, Vol. 125, 2019, pp. 246-262.
- Zhu, L., W. Q. Liu, H. Fang, J. Y. Chen, Y. Zhuang, and J. Han. Design [36] and simulation of innovative foam-filled Lattice Composite Bumper System for bridge protection in ship collisions. Composites Part B-Engineering, Vol. 157, 2019, pp. 24-35.
- Wang, F., H. J. Chang, B. H. Ma, Y. G. Wang, L. M. Yang, J. Liu, et al. Flexible guided anti-collision device for bridge pier protection against ship collision: Numerical simulation and ship collision field test. Ocean Engineering, Vol. 271, 2023, id. 113696.

- [38] Han, J., L. Zhu, H. Fang, J. Wang, and P. Wu. The energy absorption behavior of novel composite sandwich structures reinforced with trapezoidal latticed webs. *Reviews on Advanced Materials Science*, Vol. 60, 2021, pp. 503–518.
- [39] Yan, H. F., H. Fang, L. Zhu, E. S. Jia, Z. W. Dai, and X. C. Zhang. Evaluation of a novel steel box-soft body combination for bridge protection against ship collision. *Reviews on Advanced Materials Science*, Vol. 62, 2023, id. 0295.
- [40] ASTM D3039/D3039M-14. Standard test method for tensile properties of polymer matrix composite materials, ASTM, PA, USA, 2014.
- [41] ASTM D3518/D3518M-94. Standard test method for in-plane shear response of polymer matrix composite material by tensile test of a ±45°, ASTM, PA, USA, 1994.
- [42] ASTM D3410/D3410M-16. Standard test method for compressive properties of polymer matrix composite materials with unsupported gage section by shear loading, ASTM, PA, USA, 2016.
- [43] ASTM D695-15. Standard test method for compressive properties of rigid plastics, ASTM, PA, USA, 2015.
- [44] ASTM D3039/D3039M-17. Standard test method for tensile properties of polymer matrix composite materials, ASTM, PA, USA, 2017.